Supporting information

Overcoming challenges in ^{67}Zn NMR: a new strategy of signal enhancement for MOF characterization

Wanli Zhang [a], Alia Hassan [b], Jochem Struppe [c], Martine Monette [d], Ivan Hung [e], Zhehong Gan [e], Vinicius Martins [a], Victor Terskikh [f], Yining Huang [a*]

[a] *Department of Chemistry, University of Western Ontario, London, Ontario, Canada N6A 5B7.*

[b] *Bruker Switzerland AG, Fällanden, Switzerland.*

[c] *Bruker Biospin Corporation, 15 Fortune Drive, Billerica, MA 01821, USA.*

[d] *Bruker Biospin Ltd., 2800 High Point Drive, Suite 206, Milton, Ontario L9T 6P4, Canada.*

[e] *National High Magnetic Field Laboratory, 1800 East Paul Dirac Drive, Tallahassee, Florida 32310, USA.*

[f] *Metrology, National Research Council Canada, Ottawa, Ontario K1A 0R6, Canada.*

* Corresponding author; YH email: yhuang@uwo.ca,

Table of contents

1. Experimental details for sample preparation and characterization

Sample preparation. All reagents and solvents were commercially available and used without further purification.

ZIF-4.[1] $Zn(CH_3COO)_2 \bullet 2H_2O$ (0.22 g, 1.0 mmol) and imidazole (0.20 g, 3.0 mmol) were dissolved in DMF (15 mL) in a 30 mL Teflon-lined stainless-steel autoclave. The autoclave was then sealed and heated at 120 °C for 72 h. After cooling to room temperature naturally, the solid products were collected by filtration and washed with DMF followed by ethanol three times.

Microporous α-$Zn_3(HCOO)_6$.[2] In a 100 mL glass vessel, a well-mixed solution of 25.0 mL methanol, 1.6 mL formic acid, and 4.2 mL triethylamine was added dropwise into a solution containing 25 mL methanol and 3.0 g of $Zn(NO_3)_2 \cdot 6H_2O$. The jar was then covered by parafilm and small holes were pinned to allow for slow evaporation of methanol at room temperature. Colorless, transparent crystals were collected with vacuum filtration after 3 days and washed with methanol.

Powder X-ray diffraction patterns. PXRD patterns were obtained using a Rigaku diffractometer with Cu Kα radiation (λ = 1.5406 Å). 2θ values were set to range from 5 to 45° with an increment of 0.02° and a scanning rate of 5° min^{-1}.

Solid-state NMR measuerments. ^{67}Zn solid-state NMR experiments were performed on a Bruker NEO-800 at 18.8 T ($\nu_0(^{67}Zn)$ = 50.05 MHz) at the Bruker application lab (Fällanden, Switzerland). All the experiments (1D MAS and 2D

3QMAS) were carried out by using a broadband 3.2 mm CPMAS cryoprobe. This cryoprobe is in HX configuration, where the frequency range of X channel spans from ^{15}N to $^{47/49}Ti$ on the 800 MHz spectrometer. The probe is designed for 3.2 mm MAS rotors with a design differing significantly from conventional 3.2 mm MAS probe. The rotors used for cryoprobe are slightly longer than the conventional 3.2 mm rotors. Thus, the volume is larger and more similar to that of a conventional 4 mm rotor. The maximum spinning speed of this cryoprobe is 20 kHz. The probe's rf coil and preamplifier are cooled down to cryogenic temperatures to significantly reduce thermal noise and, therefore, enhance SNR. Note that although the sample coil, rf circuit and electronics are operated at cryogenic temperatures, the sample is thermoregulated independently. The sample temperature can be regulated between -20 and 60 ^{o}C. The 1D MAS spectra were acquired with a Hahn-echo sequence [(π/2)-τ-π-τ-acq]. The π/2 and π pulse lengths were 4.16 and 8.32 μs, respectively. The spinning rate was at 15 kHz and the ^{1}H decoupling field was 50 kHz. The recycle delay was 0.25 s. Total numbers of transients for 1D experiments are 32,768 and 8,192 for ZIF-4 and α-$Zn_3(HCOO)_6$, respectively. The ^{67}Zn 3QMAS spectra were obtained by using double frequency sweeps (DFS) for signal enhancement[3,4] with a split-t_1 approach[5] and the same decoupling power (50 kHz). A starting frequency of 30 kHz, a frequency sweep of 500 kHz and a timing resolution of 40 ns produced a DFS shape pulse set to 2 rotor periods (133.33 μs). The carrier was set off resonance from the Hahn Echo spectrum (350 ppm), for the 3QMAS experiments. As a result, an offset of 4 kHz was set for selective pulse. Employing Apodization Weighted Sampling (AWS) for further signal enhancement[6] resulted in highly resolved 3QMAS spectra. The t_1 increments were 42 and 72, resulting in acquisition times of 3 days and 4.5 hours, and 3 days and 19 hours for

ZIF-4 and microporous α-$Zn_3(HCOO)_6$, respectively. The transient numbers of each slice are 48,960 and 33,600 for ZIF-4 and α-$Zn_3(HCOO)_6$, respectively. A spectral width of 7500 Hz and a pulse delay of 0.25 s were used for the 3QMAS experiments of both MOFs. The use of DFS for additional sensitivity enhancement is important as it increases the signal by a factor of 2.4 compared to the 3QMAS without DFS.

^{67}Zn 1D MAS NMR spectrum of ZIF-4 at 35.2 T was acquired using a one-pulse sequence with a pulse delay of 0.05 s and 74,752 transients.

All ^{67}Zn NMR spectra were referenced to saturated $Zn(NO_3)_2$ solution at 0 ppm.[7] For discussion, ^{67}Zn 1D MAS spectra of ZIF-4 and microporous α-$Zn_3(HCOO)_6$ at 21.1 T which were reported previously[8,9] are also included. Detailed experimental parameters at three magnetic fields (18.8, 21.1 and 35.2 T) are given in Table S1 and Table S2.

NMR spectral simulations. ssNake NMR software package[10] was used to simulate the 1D MAS NMR spectra and extract the δ_{iso} and P_Q values from 3QMAS spectra.

Extracting NMR parameters from 3QMAS spectra.

ZIF-4. The line-shapes of the two signals taken along the F2 cross-sections are very well defined. Therefore, their C_Q, η_Q, and δ_{iso} values were extracted by directly fitting the F2 cross sections. These values were then used as initial inputs for fitting the 1D MAS spectra for further refinement.

Microporous α-$Zn_3(HCOO)_6$. This MOF has four inequivalent Zn sites. Consequently, although four peaks are separated, the SNR of each signal along F2 cross section is low, making it difficult to directly obtaining the NMR parameters for each site via simulation. Instead, the isotropic chemical shift, δ_{iso} (in ppm) and the quadrupolar product, $P_Q = C_Q(1 + \eta_Q^2/3)^{1/2}$ (in MHz) for each site were derived from δ_1 (in ppm) along the F1 dimension and the spectral center of gravity (δ_2 in ppm) along the F2 dimension. The δ_2 value of each site can be conveniently extracted by using software package ssNake.[10] δ_{iso} and P_Q are related to δ_1 and δ_2 via the following equations[11]:

$$\delta_{iso} = \frac{17}{27}\delta_1 + \frac{10}{27}\delta_2$$

$$P_Q = \left\{\frac{170}{81}\frac{[4I(2I-1)]^2}{[4I(I+1)-3]}(\delta_1 - \delta_2)\right\}^{1/2} \nu_0 \times 10^{-3}$$

where ν_0 is the Larmor frequency and I is the spin quantum number. Note that the δ_{iso} and P_Q values can be determined accurately from the resonance positions in F1 and F2 dimensions without the need of fitting the F2 cross section under the SNR obtained.

Plane-wave DFT calculations. The plane-wave periodic calculations on the ^{67}Zn magnetic shielding and electric field gradient (EFG) tensor parameters were performed with the CASTEP 19 code.[12] Calculations were performed on the ComputeCanada/Sharcnet clusters (https://www.sharcnet.ca/). Perdew, Burke, and Ernzerhof (PBE) functionals[13] were employed in the generalized gradient approximation (GGA) for the exchange correlation energy for all calculations with a plane-wave basis set cutoff energy of 800 eV. Convergence tolerance parameters in geometry optimization have been set as follows: energy, 10^{-5} eV/atom;

maximum force, 0.03 eV/ Å; maximum stress, 0.05 GPa; maximum displacement, 10^{-3} Å. NMR parameters were calculated using "on-the-fly" ultrasoft pseudopotentials provided with the projector augmented-wave method (GIPAW). Since the CASTEP code computes the total shielding of ^{67}Zn, the conversion to chemical shift was performed using the approach described in the literature[14]. The computation of cubic ZnS gave a total shielding of 1231 ppm corresponding to the experimental shift of 381 ppm[15] relative to 1 M $Zn(NO_3)_2$. Therefore, the $\delta_{iso}(^{67}Zn)$ values were calculated by using the relationship $\delta_{iso}(^{67}Zn) = 1612 - \sigma_{iso}(^{67}Zn, CASTEP)$ (in ppm). C_Q is obtained with $C_Q = V_{zz}Q(^{67}Zn)/\hbar$ ($Q(^{67}Zn)$ = 122 mb[16]). The EFG tensor is visualized with the *MagresView* code[17].

DFT model cluster calculations. Ab initio calculations of the clusters were carried out using the Gaussian 16 program[18] running on SHARCNET (www.sharcnet.ca). The EFG and the magnetic shielding tensors of ^{67}Zn in all model clusters were calculated using hybrid density functional theory (DFT) at the B3LYP level of theory using the GIAO method. The basis sets used were 6-311G* for Zn atoms, 6-311+G* for N or O atoms bonded directly to Zn atoms and 6-31G* for other atoms. These basis sets were chosen based on previous studies[19,20], which showed good agreement with experimental values. The calculated ^{67}Zn isotropic magnetic shielding (σ_{iso}) values were converted into the chemical shifts (δ_{iso}) using the absolute shielding scale for ^{67}Zn derived from optical pumping and nonrelativistic calculations with $\delta_{iso}(^{67}Zn) = 1831.67 - \sigma_{iso}(^{67}Zn, Gaussian)$ (in ppm)[21]. 1831.67 ppm is the absolute shielding constant of an infinitely dilute Zn^{2+} ion in D_2O at 303 K. The EFG tensor is visualized with the *EFGShield* software package[22].

2. Additional information on two MOF based materials.

ZIF-4. ZIF-4 crystallizes in the orthorhombic space group *Pbca*. Each Zn^{2+} ion is tetrahedrally bound to 4 nitrogen atoms in four different imidazolate linkers and each linker bridges two crystallographically inequivalent Zn^{2+} sites via the 1,3-positions of the imidazolate ligand to form 3D framework with *cag* network topology (Fig. 1a). The framework contains the cages with a diameter of about 5 Å. The size of the window via which the guest gains access is rather small, i.e. ~ 2.1 Å (Fig. 1a), but the orientation of the organic linker can change upon adsorption, opening the "gate" for gas adsorption.[23] ZIF-4 undergoes phase transitions to dense or amorphous phases and exhibits breathing phenomenon upon stimulated by high temperature and high pressure.[24,25] Due to these structural properties, ZIF-4 finds many applications. For example, it can be used for gas adsorption/separation (H_2, N_2, CO_2, CH_4 etc.),[26,27] and the framework of anode materials for lithium-ion batteries[28]. It is one of the few ZIFs that can be made into technologically important ZIF-glasses.[29]

Microporous α-$Zn_3(HCOO)_6$. Microporous α-$Zn_3(HCOO)_6$ belongs to a family of microporous MOFs constructed from formate linkers, $M_3(HCOO)_6$ (M = Mg, Zn, Mn, Co, Ni, and Fe)[30] and has shown great potential as gas capture media[8]. Microporous α-$Zn_3(HCOO)_6$ crystallizes in the monoclinic system (space group $P2_1/n$) with four inequivalent Zn sites in the unit cell.[2] The crystal structure reported in the literature indicates that the four inequivalent octahedral Zn sites can be classified into three groups of chemically inequivalent Zn sites: (1) Zn1 is bound to six μ_2 oxygens (O1, O3, O5, O7, O9, and O11) where each oxygen coordinates to two Zn atoms; (2) Zn2

is coordinated to four μ_2 (O1, O3, O5, O7) and two μ_1 oxygens (O2, O12, each μ_1 oxygen is bound to only a single Zn atom); and (3) Zn3 and Zn4 each bond to two μ_2 and four μ_1 oxygens (Zn3 is connected to two μ_2 (O9, O9) and four μ_1 (O4, O4, O6, O6); Zn4 connected to two μ_2 (O11, O11) and four μ_1 (O8, O8, O10, O10) atoms). Although Zn3 and Zn4 are chemically equivalent, they are crystallographically inequivalent as they each coordinate to different μ_2-O and μ_1-O sites. The four sites have the relative occupancies of Zn1:Zn2:Zn3:Zn4 = 2:2:1:1.

3. Additional results and discussion

Discussion on SNR of three ^{67}Zn 1D MAS spectra acquired at 18.8, 21.1 and 35.2 T. Since three 1D MAS spectra shown in Fig. 2 were measured at different facilities over a long period of time, their acquisition parameters are very different (Table S1), which makes a signal-to-noise ratio (SNR) comparison only semi-quantitative. In an attempt to compare the spectra, we processed them by truncating their free induction decays (FIDs) to the same acquisition time of 2.56 ms (the actual value used at 18.8 T) before Fourier transformation. This allowed us to negate differences in the spectral widths used. The SNR thus obtained for the spectra at 35.2, 21.1, and 18.8 T are 148, 20, and 41, respectively. However, the number of transients accumulated for the three spectra are different. Therefore, a more apt comparison requires that the SNR be scaled by the square root of the number of scans. This yields *SNR*(*n*) values of 0.54, 0.11 and 0.23 for the spectra acquired at 35.2, 21.1, and 18.8 T. There remain a number of experimental parameters which may affect the SNR and cannot be mitigated post hoc via spectral processing or scaling. For example, the 21.1 T data was acquired using a 7-mm MAS probe which can

accommodate a much larger amount of sample compared to the other spectra acquired with 3.2-mm probes; the SNR at 21.1 T would be reduced if scaled by the sample mass. The 18.8 T data was acquired using a Hahn-echo pulse sequence, whereas a one-pulse sequence was employed for the other two spectra. The intensity of the echo spectrum may be lower than that of the one-pulse spectrum due to the effect of T_2. A higher SNR would be expected if a one-pulse sequence were used at 18.8 T. The spectra were acquired with different relaxation delays. We believe that the ^{67}Zn nuclei achieved full relaxation in all instances but were unable to verify quantitatively due to limitations in spectrometer time. The dead time associated with probe ringing is another factor. Even with these complications, from the *SNR*(*n*) values obtained, it is clear that cryoprobe and ultrahigh magnet technologies both provide significant signal enhancement for half-integer quadrupolar nuclei.

ZIF-4: plane-wave DFT calculations for spectral assigmnements. To assign the two resonances to the Zn sites in the unit cell, gauge-including projector augmented wave (GIPAW) DFT calculations were performed on the extended periodic structure of ZIF-4 using CASTEP code.[12] Specifically, the ^{67}Zn EFG parameters were calculated on two structures: (1) X-ray crystal structure without optimization (XRD structure); (2) the structure with optimized atomic positions for all the atoms within the unit cell (fully-optimized structure). Plane-wave DFT calculations based on both structures replicate the C_Q values fairly well (Table S4) and clearly show that C_Q of Zn1 is consistently larger than that of Zn2. The calculations using fully-optimized structure predict C_Q values to the highest degree of accuracy. Based on the calculated quadrupolar coupling constants, the resonance with larger C_Q is assigned

to Zn1. This assignment is also consistent with that reported previously based on model cluster calculations.[9] The larger C_Q of Zn1 is attributed to higher degree of distortion of the ZnN_4 tetrahedron.

Microporous α-$Zn_3(HCOO)_6$: plane-wave DFT calculations for spectral assigmnement. To assign the four ^{67}Zn resonances to four inequivalent Zn sites, plane-wave DFT calculations were performed to calculate ^{67}Zn EFG and the magnetic shielding tensors. The NMR parameters were calculated using three structures: XRD structure, fully-optimized structure and a structure obtained by geometry optimization of all linker atoms (C, H and O) termed linker-optimized structure. The results are given in Table S7. Since for the 4 inequivalent Zn sites in this MOF, the experimentally obtained C_Q values are all very similar (Table S6), the calculated isotropic chemical shift values were then utilized to assign the four resonances. Although plane-wave DFT calculations predict the δ_{iso} values that somewhat depend on the structure used, the order of calculated δ_{iso} values is independent of the structure model: δ_{iso}(Zn2)> δ_{iso}(Zn1)> δ_{iso}(Zn4)> δ_{iso}(Zn3). This order was, therefore, used for spectral assignment. Specifically, the signal, S4 with the lowest observed δ_{iso} of -46 ppm (δ_1 = -14 ppm) is assigned to Zn3; the resonance with the highest experimental δ_{iso} of 10 ppm (δ_1 = 35 ppm) to Zn2; the peak with the second highest δ_{iso} of 5 ppm (δ_1 = 30 ppm) to Zn1. Among three structure models used, plane wave DFT calculations of the EFG tensor parameters incorporated geometry optimization of all light atoms (C, H, and O), i.e. linker-optimized structure overall give a better predictions of C_Q and η_Q values, implying that linker position is important to the predication of the EFG.

4. Refinement of Zn local structures in microporous α-$Zn_3(HCOO)_6$.

A comparison of calculated C_Q values in Table S7 with experimentally determined ones (Table S6) reveals that the calculated C_Q of Zn1 is consistently larger than the observed value. To exploit the correlation between the EFG parameters and local geometry around this particular Zn site, the DFT calculations using a simple cluster model (Fig. S5) were carried out. The calculation results indicate that the largest component of the EFG tensor, the V_{zz} is closely aligned with the Zn1-O5 bond (the angle between V_{zz} and the Zn-O5 bond is merely 7.38°, Fig. S6(a)). The bond length of the Zn1-O5 and bond angle of the O7-Zn-O5 were then systematically varied to examine the effect of these parameters on C_Q. As illustrated in Fig. S6(a), the C_Q value is much more sensitive to the Zn1-O5 bond length than the O-Zn-O bond angle. A slight reduction in bond length leads to a rapid decrease in C_Q. On the other hand, the C_Q value is much less sensitive to the changes in bond angle. It appears that the actual Zn1-O5 bond length is slightly shorter than 2.125 Å reported in the XRD structure. The plane-wave DFT calculations using the linker-optimized structure underestimates the C_Q value of Zn2. The V_{zz} direction at Zn2 aligns approximately with the Zn2-O12 bond with the angle between the two being 19.6°. The cluster calculations show that similar to the case for Zn1, the C_Q value of Zn2 varied significantly with the Zn2-O12 bond length and are insensitive to the O-Zn-O bond angle. However, unlike the situation for Zn1 where the C_Q increases with the Zn-O1 bond length monotonically, the C_Q value of Zn2 has a minimum value at the Zn2-O12 bond length of 2.09 Å (Fig. S6 (b)). A slight decrease in the Zn2-O12 from 2.041 to 2.02 Å leads to an increase in the C_Q approaching the experimental value (4.5 MHz). On the other hand, to reach the same C_Q, a significant increase in the Zn2-O12 distance to 2.19 Å was required, suggesting a fairly large error in X-ray

structure, which is unlikely. Furthermore, the Zn-O distances in MOFs are usually in the range between 2.02 - 2.15 Å. Therefore, it is not unreasonable to assume that the actual Zn2-O12 bond length is only slightly shorter than the one in XRD structure.

5. Additional advantages of CPMAS cryoprobe.

The low-gamma cryogentic MAS probe technology has several additional advantages for NMR of unreceptive half-integer quadrupolar nuclei including ^{67}Zn. For example, this 3.2 mm CryoProbe™ has a large sample volume because this rotor is slightly longer than the conventional 3.2 mm rotor. Thus, the volume is larger and actually similar to that of a conventional 4 mm rotor. The maximum spinning speed of this probe is 20 kHz, which is comparable to the spinning rate of 24 kHz for a conventional 3.2 mm probe. It also has a higher *Q* factor (resulting from coil being cooled to cryogenic temperature) than the conventional probe operating at room temperature and, consequently, is able to generate a stronger B_1 field despite of the larger coil size to accommodate coil cooling. This is particularly beneficial to MQMAS experiments. Although the probe design is rather complicated, it fits into a narrow bore magnet, permitting it to be used at the instrument operating at very high magnetic fields (e.g. 1.2 GHz). The robust design of the probe permits running experiments continuously for extended periods of time (days and weeks), which is important to unreceiptive nuclei for signal averaging.

6. Additional figures and tables.

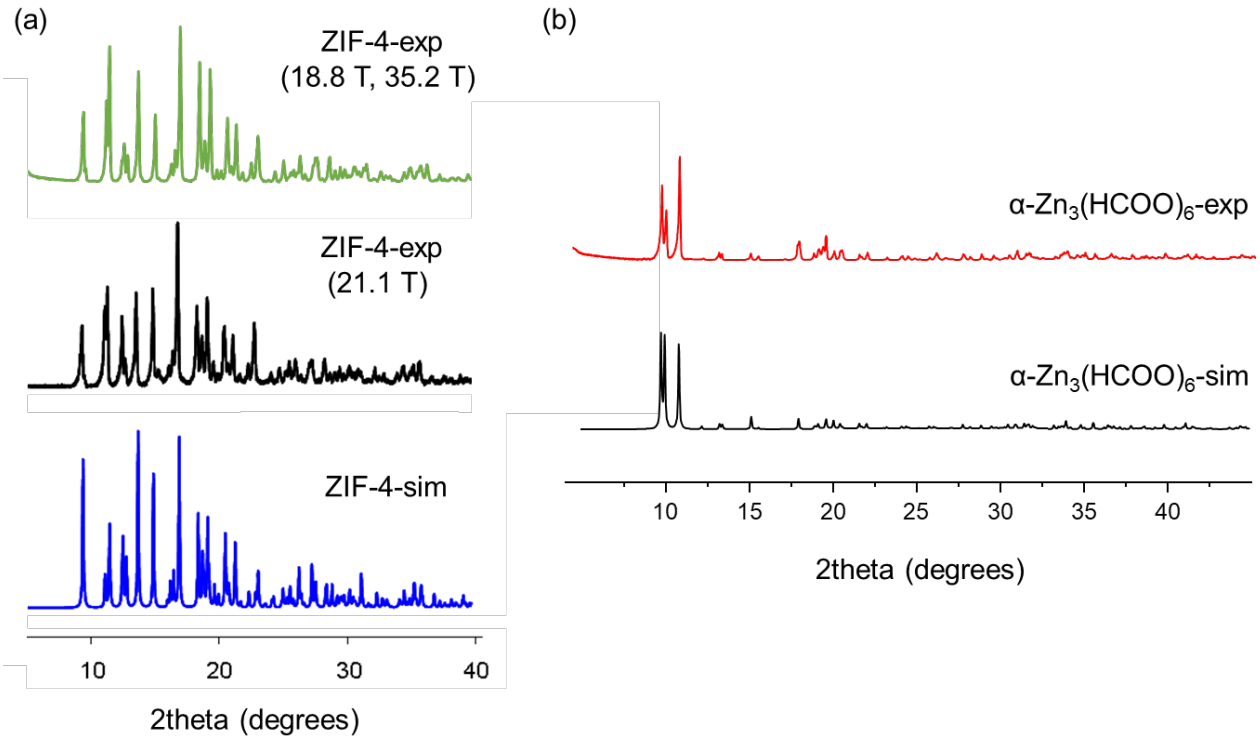

Fig. S1 (a) Experimental and simulated PXRD patterns of ZIF-4 samples used at 18.8 , 35.2 and 21.1 T. (b) Experimental and simulated PXRD patterns of microporous α-$Zn_3(HCOO)_6$ sample used at 18.8 and 21.1 T.

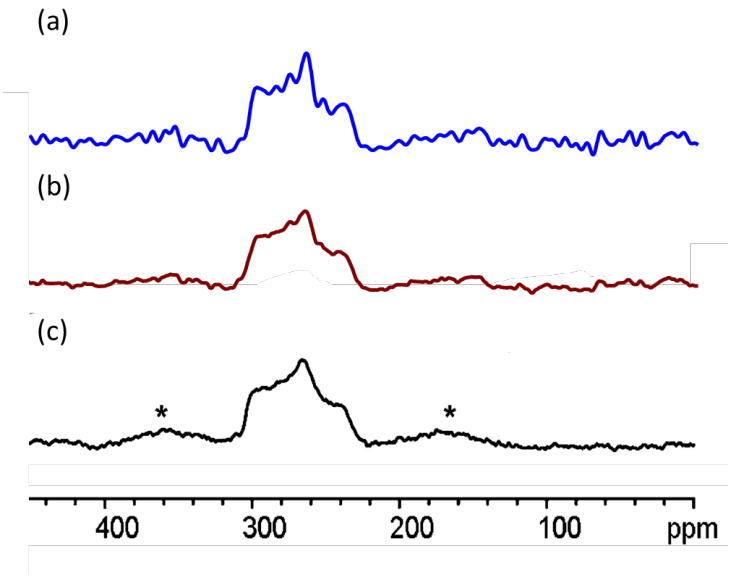

Fig. S2 A comparison of the ^{67}Zn 1D MAS NMR spectra of ZIF-4 at 21.1 T processed differently: (a) FID being truncated to 2.56 ms and no line-broadening applied; (b) without truncation and with a line-broadening of 200 Hz; (c) taken from *Chem. Eur. J.*, 2012, **18** 12251.

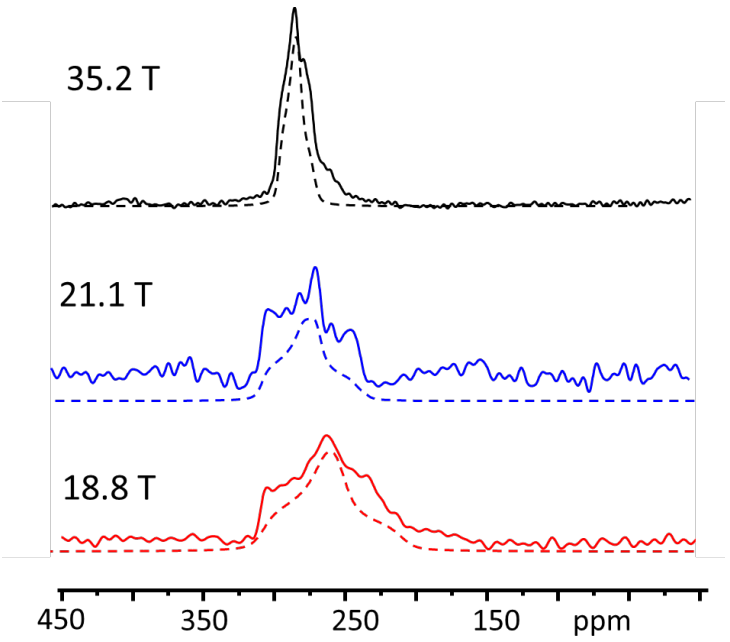

Fig. S3 Simulations of ^{67}Zn 1D MAS NMR spectra (dash) of ZIF-4 using a single Zn site (δ_{iso} = 300(9) ppm, C_Q = 3.8(2) MHz, η_Q = 0.85(10)).

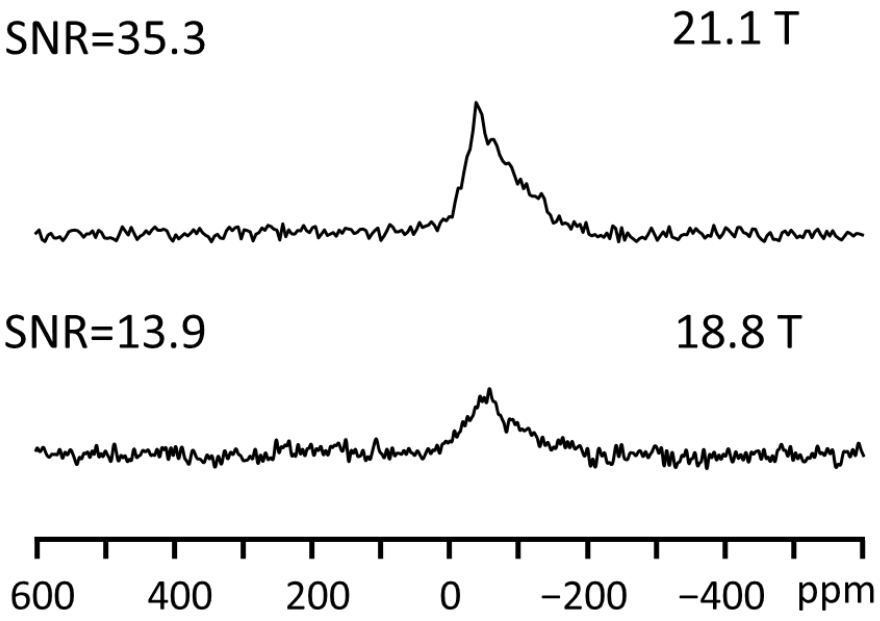

Fig. S4 ^{67}Zn MAS spectra of microporous of α-$Zn_3(HCOO)_6$ at 21.1 and 18.8 T. The FIDs of the spectra at both fields were truncated to 4.1 ms (the actual value at 21.1 T) to equalize the noise level between the spectra. The spectra were then processed with a line-broadening of 100 Hz. The SNRs for the spectra at 21.1 : 18.8 T = 35.3 : 13.9 (i.e. 2.5 : 1).

Since the numbers of transients accumulated are 589,824 and 8,192 at 21.1 and 18.8 T, respectively, the SNR was then scaled by the square root of the number of scans, yielding that the ratio of SNR/$\sqrt{n}$ for the spectra acquired at 21.1 and 18.8 T is 0.29 : 1. Note that the calculation of SNR/$\sqrt{n}$ of the spectrum at 21.1 T did not take some signal loss due to the use of modified Hahn-echo (90°-90°) sequence into consideration.

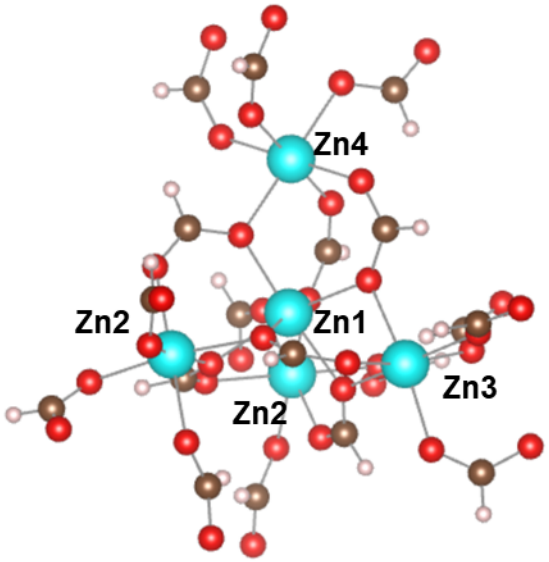

Fig. S5 Illustration of the $[Zn_5(HCOO)_{18}]^{8-}$ cluster used for the EFG tensor calculations.

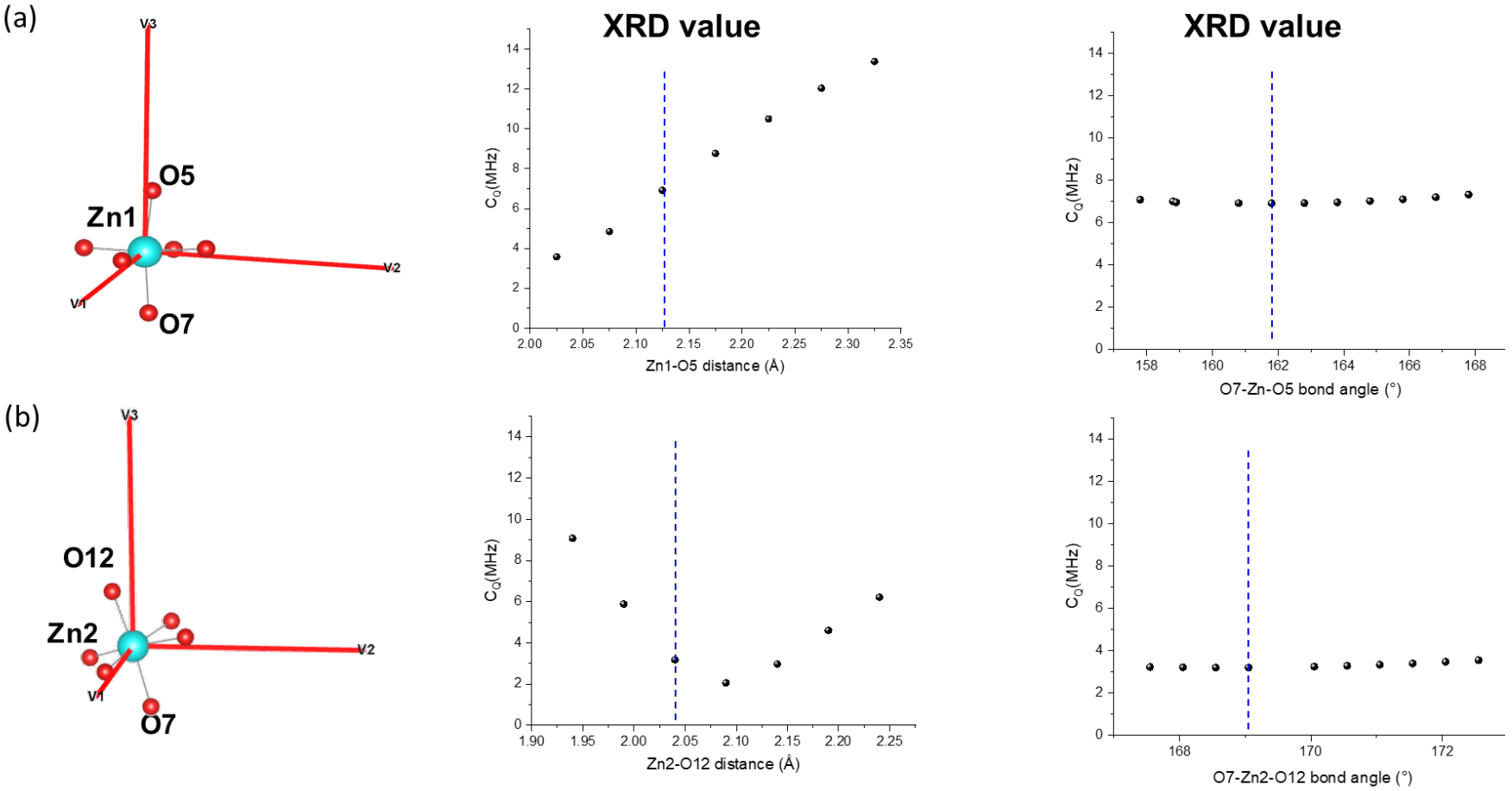

Fig. S6 (a) The EFG tensor directions at Zn1, and the correlations between the calculated C_Q and the Zn1-O5 bond length and O7-Zn1-O5 bond angle. The angle between V_{zz} and the Zn-O5 bond is 7.38°, (b) The EFG tensor directions at Zn2 (the V_{zz} direction at Zn2 aligns approximately with the Zn2-O12 bond with the angle between the two being 19.6°), the correlations between the calculated C_Q and the Zn2-O12 bond length and O7-Zn2-O12 bond angle.

Table S1. ^{67}Zn NMR experimental parameters used for acquiring 1D MAS spectra of ZIF-4 at three magnetic fields.

	18.8 T	21.1 T	35.2 T
Pulse sequence	Hahn-echo	One pulse	One pulse
Pulse delay (s)	0.25	1	0.05
Dwell (μs)	2.5	10	10
Spectral width (kHz)	200	50	50
Number of scans	32,768	36,032	74,752
Pre-scan delay (μs)	40	7	20
Size of fid (TD)	1024	2048	1024
Acquisition time	2h 23 mins	10 h	1h 15 mins
^{1}H-decoupling field (kHz)	50	25	0
Probe	3.2 mm CPMAS cryoprobe	7 mm MAS probe	3.2 mm MAS probe
Rotor size	3.2-mm	7-mm	3.2-mm
$\pi/2$ pulse width (μs)	4.2	1.5	2.0
Flip angle (°)	90	90	90
Spinning rate (kHz)	15	5	10

Table S2. ^{67}Zn NMR experimental parameters used for acquiring 1D MAS spectra of α-$Zn_3(HCOO)_6$ at two magnetic fields.

	18.8 T	21.1 T
Pulse sequence	Hahn-echo (90°-180°)	Modified Hahn-echo[a] (90°-90°)
Pulse delay (s)	0.25	0.25
Dwell (μs)	5	1
Spectral width (kHz)	100	500
Number of scans	8,192	589,824
Pre-scan delay (μs)	40	25
Size of fid (TD)	1024	4096
Acquisition time	34.1 minutes	1 day 18 hours
^{1}H-decoupling field (kHz)	50	25
Probe	3.2 mm CPMAS cryoprobe	4 mm MAS probe
Rotor size	3.2-mm	4-mm
$\pi/2$ pulse width (μs)	2.7	3.0
Flip angle (°)	90	90
Spinning rate (kHz)	15	15

[a] Modified Hahn-echo (90°-90°) pulse sequence was used at 21.1 T to ensure broader excitation and improved line-shape, but at a cost of the loss of some signal intensity.

Table S3. Experimental ^{67}Zn NMR parameters, calculated[a] C_Q values and peak assignments of ZIF-4.

Signal	δ_{iso}(ppm)	C_Q^{exp} (MHz)	η_Q	$\left\|C_Q^{cal}\right\|$	Assignment
S1	304(5)	5.0(4)	0.55(8)	4.9	Zn1
S2	302(4)	3.8(3)	0.78(5)	3.6	Zn2

[a] The C_Q values were calculated based on fully-optimized structure (see text in the SI).

Table S4. Calculated EFG parameters of ZIF-4 using plane-wave DFT method.

	$\left\|C_Q\right\|$ (MHz)	η_Q
XRD structure		
Zn1	4.1	0.80
Zn2	3.4	0.78
Full-optimized structure		
Zn1	4.9	0.59
Zn2	3.6	0.89

Table S5. Experimental ^{67}Zn NMR parameters, calculated[a] δ_{iso}^{cal} values, and peak assignments of microporous α-$Zn_3(HCOO)_6$.

Signal	δ_1 (ppm)	δ_2 (ppm)	P_Q(MHz)	δ_{iso}^{exp} (ppm)	δ_{iso}^{cal} (ppm)	Assignment
S4	-14	-102 (2)	4.8(6)	-46(3)	-105	Zn3
S3	26	-64(3)	4.9(3)	-7(2)	-92	Zn4
S2	30	-69(2)	5.1(2)	-6(1)	-81	Zn1
S1	35	-67(2)	5.2(4)	-3(2)	-67	Zn2

[a] δ_{iso}^{cal} values were calculated based on the linker-optimized crystal structure (see the text in the SI).

Table S6. Experimental ^{67}Zn NMR parameters of microporous α-$Zn_3(HCOO)_6$ obtained from simulation of 1D MAS spectra at 18.8 and 21.1 T.

Signal	δ_1 (ppm)	δ_{iso}^{exp} (ppm)	C_Q^{exp} (MHz)	η_Q^{exp}	Assignment	Intensity ratio
S4	-14	-46(9)	4.5(6)	0.65(8)	Zn3	17 %
S3	26	-7(8)	4.2(8)	1.00(9)	Zn4	17 %
S2	30	5(6)	4.6(6)	0.60(8)	Zn1	33 %
S1	35	10(10)	4.5(8)	0.95(10)	Zn2	33 %

Table S7. Calculated ^{67}Zn NMR parameters of microporous α-$Zn_3(HCOO)_6$ using plane-wave DFT method.

	δ_{iso}(ppm)	$\left\|C_Q\right\|$ (MHz)	η_Q
XRD structure			
Zn 1	-49	5.1	0.66
Zn 2	-33	4.0	0.71
Zn 3	-61	3.7	0.75
Zn 4	-58	2.9	0.95
Linker-optimized structure			
Zn 1	-81	5.7	0.74
Zn 2	-67	2.8	0.96
Zn 3	-105	4.9	0.74
Zn 4	-92	4.2	0.97
Fully-optimized structure			
Zn 1	-84	5.7	0.89
Zn 2	-68	3.2	0.77
Zn 3	-103	5.0	0.86
Zn 4	-91	3.7	0.79

Reference

1 K. S. Park, Z. Ni, A. P. Côté, J. Y. Choi, R. Huang, F. J. Uribe-Romo, H. K. Chae, M. O'Keeffe and O. M. Yaghi, *Proc. Natl. Acad. Sci. U.S.A.*, 2006, **103**, 10186.

2 Z. Wang, Y. Zhang, M. Kurmoo, T. Liu, S. Vilminot, B. Zhao and S. Gao, *Aust. J. Chem.*, 2006, **59**, 617.

3 A. Brinkmann and A. P. M. Kentgens, *J. Phys. Chem. B*, 2006, **110**, 16089.

4 R. W. Schurko, I. Hung and C. M. Widdifield, *Chem. Phys. Lett.*, 2003, **379**, 1.

5 A. P. M. Kentgens and R. Verhagen, *Chem. Phys. Lett.*, 1999, **300**, 435.

6 B. Simon and H. Köstler, *J. Biomol. NMR*, 2019, **73**, 155.

7 R. K. Harris, E. D. Becker, S. M. C. De Menezes, R. Goodfellow and P. Granger, *Pure Appl. Chem.*, 2001, **73**, 1795–1818.

8 B. Wu, Y. T. A. Wong, B. E. G. Lucier, P. D. Boyle and Y. Huang, *ACS Omega*, 2019, **4**, 4000.

9 A. Sutrisno, V. V. Terskikh, Q. Shi, Z. Song, J. Dong, S. Y. Ding, W. Wang, B. R. Provost, T. D. Daff and T. K. Woo, *Chem. Eur. J.*, 2012, **18**, 12251.

10 S. G. J. Van Meerten, W. M. J. Franssen and A. P. M. Kentgens, *J. Magn. Reson.*, 2019, **301**, 56.

11 J.-P. Amoureux, C. Huguenard, F. Engelke, and F. Taulelle, *Chem. Phys. Lett.*, 2002, **356**, 497.

12 S. J. Clark, M. D. Segall, C. J. Pickard, P. J. Hasnip, M. I. J. Probert, K. Refson and M. C. Payne, *Z Kristallogr Cryst Mater.*, 2005, **220**, 567.

13 J. P. Perdew, K. Burke and M. Ernzerhof, *Phys. Rev. Lett.*, 1996, **77**, 3865.

14 U. Werner-Zwanziger, K. W. Chapman and J. W. Zwanziger, *Z. Phys. Chem.*, 2012, **226**, 1205.

15 S. Sham and G. Wu, *Can. J. Chem.*, 1999, **77**, 1782.

16 P. Pyykkö, *Mol. Phys.*, 2018, **116**, 1328.

17 S. Sturniolo, T. F. G. Green, R. M. Hanson, M. Zilka, K. Refson, P. Hodgkinson, S. P. Brown and J. R. Yates, *Solid State Nucl. Magn. Reson.*, 2016, **78**, 64.

18 M. J. ea Frisch, G. W. Trucks, H. B. Schlegel, G. E. Scuseria, M. A. Robb, J. R. Cheeseman, G. Scalmani, V. Barone, G. A. Petersson and H. Nakatsuji, 2016.

19 R. Ida and G. Wu, *J. Phys. Chem. A*, 2002, **106**, 11234.

20 Y. Zhang, S. Mukherjee and E. Oldfield, *J. Am. Chem. Soc.*, 2005, **127**, 2370.

21 K. H. Mroué and W. P. Power, *J. Phys. Chem. A*, 2010, **114**, 324.

22 S. Adiga, D. Aebi and D. L. Bryce, *Can. J. Chem.*, 2007, **85**, 496.

23 J. Gandara-Loe, A. Missyul, F. Fauth, L. L. Daemen, Y. Q. Cheng, A. J. Ramirez-Cuesta, P. I. Ravikovitch and J. Silvestre-Albero, *J. Mater. Chem. A*, 2019, **7**, 14552.

24 T. D. Bennett, A. L. Goodwin, M. T. Dove, D. A. Keen, M. G. Tucker, E. R. Barney, A. K. Soper, E. G. Bithell, J.-C. Tan and A. K. Cheetham, *Phys. Rev. Lett.*, 2010, **104**, 115503.

25 S. Henke, M. T. Wharmby, G. Kieslich, I. Hante, A. Schneemann, Y. Wu, D. Daisenberger and A. K. Cheetham, *Chem. Sci.*, 2018, **9**, 1654.

26 A. Battisti, S. Taioli and G. Garberoglio, *Microporous and Mesoporous Mater.*, 2011, **143**, 46.

27 M. Hartmann, U. Böhme, M. Hovestadt and C. Paula, *Langmuir*, 2015, **31**, 12382.

28 J. Chai, K. Wang, Q. Li, J. Du, L. Jiang, N. Han, W. Zhang, B. Tang and Y. Rui, *J. Alloys Compd.*, 2022, **914**, 165316.
29 R. S. K. Madsen, A. Qiao, J. Sen, I. Hung, K. Chen, Z. Gan, S. Sen and Y. Yue, *Science*, 2020, **367**, 1473.
30 Z. Wang, B. Zhang, Y. Zhang, M. Kurmoo, T. Liu, S. Gao and H. Kobayashi, *Polyhedron*, 2007, **26**, 2207.